Journal Pre-proofs

Electrospinning/Electrospraying coatings for metal microneedles: a design of experiments (DOE) and Quality by Design (QbD) approach

Radeyah Ali, Prina Mehta, Paraskevi Kyriaki Monou, Muhammad S. Arshad, Emmanuel Panteris, Manoochehr Rasekh, Neenu Singh, Omar Qutachi, Philippe Wilson, Dimitrios Tzetzis, Ming-Wei Chang, Dimitrios G. Fatouros, Zeeshan Ahmad

PII: S0939-6411(20)30267-8
DOI: https://doi.org/10.1016/j.ejpb.2020.08.023
Reference: EJPB 13403

To appear in: *European Journal of Pharmaceutics and Biopharmaceutics*

Received Date: 19 March 2020
Revised Date: 11 August 2020
Accepted Date: 24 August 2020

Please cite this article as: R. Ali, P. Mehta, P. Kyriaki Monou, M.S. Arshad, E. Panteris, M. Rasekh, N. Singh, O. Qutachi, P. Wilson, D. Tzetzis, M-W. Chang, D.G. Fatouros, Z. Ahmad, Electrospinning/Electrospraying coatings for metal microneedles: a design of experiments (DOE) and Quality by Design (QbD) approach, *European Journal of Pharmaceutics and Biopharmaceutics* (2020), doi: https://doi.org/10.1016/j.ejpb.2020.08.023

Electrospinning/Electrospraying coatings for metal microneedles: a design of experiments (DOE) and Quality by Design (QbD) approach

Radeyah Ali[1], Prina Mehta[1], Paraskevi Kyriaki Monou[2] Muhammad S. Arshad[1], Emmanuel Panteris[3], Manoochehr Rasekh[1], Neenu Singh[1], Omar Qutachi[1], Philippe Wilson[4], Dimitrios Tzetzis[5], Ming-Wei Chang[6], Dimitrios G. Fatouros[2], Zeeshan Ahmad[1,*]

[1]Leicester School of Pharmacy, De Montfort University, Leicester, LE1 9BH, UK

[2]Department of Pharmaceutical Technology, School of Pharmacy, Aristotle University of Thessaloniki, Greece.

[3]Department of Botany, School of Biology, Aristotle University of Thessaloniki, GR-54124 Thessaloniki, Greece

[4]School of Animal, Rural and Environmental Sciences, Nottingham Trent University, Brackenhurst Campus, Southwell, NG25 0QF

[5]School of Science and Technology, International Hellenic University, Thermi, Greece

[6]Nanotechnology and Integrated Bioengineering Centre, University of Ulster, Jordanstown Campus, Newtownabbey, BT37 0QB, Northern Ireland, UK

Corresponding authors:

Prof. Dimitrios G. Fatouros e-mail: dfatouro@pharm.auth.gr

Prof. Zeeshan Ahmad e-mail: zahmad@dmu.ac.uk

Abstract

The research presented here shows QbD implementation for the optimisation of the key process parameters in electrohydrodynamic atomisation (EHDA). Here, the electrosprayed nanoparticles and electrospun fibers consisting of a polymeric matrix and dye. Eight formulations were assessed consisting of 5% w/v of polycaprolactone (PCL) in dichloromethane (DCM) and 5% w/v polyvinylpyrrolidone (PVP) in ethanol. A full factorial DOE was used to assess the various parameters (applied voltage, deposition distance, flow rate). Further particle and fiber analysis using Scanning Electron Microscopy (SEM), Differential Scanning Calorimetry (DSC), Thermogravimetric Analysis (TGA), Fourier Transform Infrared Spectroscopy (FTIR), particle/fiber size distribution. In addition to this *in vitro* release studied were carried out using fluorescein and Rhodamine B as model dyes and *in vitro* permeation studies were applied. The results show a significant difference in the morphology of resultant structures as well as a more rapid release profile for the PVP particles and fibers in comparison to the sustained release profiles found with PCL. *In vitro* drug release studies showed 100% drug release after 7 days for PCL particles and showed 100% drug release within 120 min for PVP particles. The release kinetics and the permeation study showed that the MN successfully pierced the membrane and the electrospun MN coating released a large amount of the loaded drug within 6 h. This study has demonstrated the capability of these robust MNs to encapsulate a diverse range drugs within a polymeric matrix giving rise to the potential of developed personalised medical devices.

Keywords: Electrohydrodynamic atomisation, quality by design, transdermal delivery, microneedles

1. Introduction

Quality by Design (QbD) involves taking a "systematic approach to development with pre-defined objectives" focussing more on the product and processes based on science and risk management [1,2]. A quality target product profile (QTPP) is established which includes and defines all requirements that the final product is expected to meet and satisfy (e.g. dosage form, strength, purity limits etc). Critical quality attributes (CQAs) of a product and their potential interaction and impact during the manufacturing process are also key [3] and are often associated with the design of the drug substance and the manufacturing process. It is from identifying CQAs that a fitting limit/range is assigned to each to make sure that the desired product quality is achieved. Critical process parameters (CPPs) are factors which heavily impact the manufacturing process and therefore need to be controlled and monitored throughout.

Electrohydrodynamic atomisation (EHDA) is a structure fabrication method that utilises an electrical field to atomise liquids [4]. Branches of EHDA include; electrospraying (ES; for particles), electrospinning (ESP; for fibers) [5,6] and electrohydrodynamic bubbling (for bubble related structures) [7,8]. ES has evolved from basic concepts [9,10] to being applied to polymers [7], ceramics [11], cosmetics [12], antibiotics [13], insulin delivery [14], food industry [15], capsules [16,17], anticancer drug delivery [18], brain drug delivery [19], buccal drug delivery [19], tissue engineering [8], biomedical engineering application using hydroxyapatite [21,22,2the 3,24] and emerging drug delivery [25]. This engineering method has evolved to enable development of new drug delivery devices such as contact lenses [26], patches [27] and stents [28]. EHDA is a non-conventional solvent-based method, which, depending on formulation properties, can be referred to as ES or ESP [29].

Several transdermal drug delivery strategies aim to enhance patient compliance when compared to conventional routes [30] and also avoid first pass drug hepatic/gastrointestinal metabolism [31]. The skins' formidable barrier, the stratum corneum (SC, ca.10-20 μm thick), has proven challenging to overcome [32]. However, transdermal microneedles (MNs) propose an appealing alternative to hypodermic needles and oral medication with potential applications with chronic complications like cancer, diabetes and Alzheimer's as well as monitoring systems for lithium levels as EEG probes [33]. These devices are less invasive, more efficient and more patient friendly [34]. They generally consist of arrays/patterns of individual solid needles measuring 50-900 μm high and having a surface density around 2000 needles/cm^2; penetrating the SC in a painless manner [35,36]. Many therapeutic agents can be delivered via the MN approach including macromolecules [37, 38], anticancer agents [39] and other hydrophilic and hydrophobic compounds [40].

One of the earliest studies demonstrating EHDA as a viable technique to produce smart MNs for drug delivery varied EHD process parameters to generate particles (100 nm to 3 μm) and fibers (400 nm to 1 μm) [41].

Both organic and inorganic composite MNs have shown capability of releasing API following skin insertion [42]. FDA-approved synthetic biodegradable and water-soluble polymers including poly-vinylpyrrolidone (PVP) and poly-caprolactone (PCL) [43] have been identified as potential matrices for drugs and successfully exploited as encapsulated agents. Reksammunadar et al demonstrated successful encapsulation of α-carotene (1 wt. %) within a PVP (10 wt. %) matrix through ESP. These composite nanofibers exerted the greatest antioxidant activity [44]. A study by Ronnander et al showed that sumatriptan succinate encapsulated in PVP dissolving MNs (DMNs) exhibited rapid drug release [36]. Whilst drugs encapsulated within a PVP matrix

demonstrate rapid release, drug loaded PCL MNs tend to show a more sustained release profile. Anderson et al supports this as the *in vitro* release of PCL MNs loaded with furosemide by diffusion was within 18 h at 37 ^{o}C [45].

This study focuses on the detailed evaluation of polymeric MN arrays coated using EHDA. Polymeric formulations and the resultant particular and fibrous structures were assessed. *In vitro* release, thermal, spectroscopic analysis, wettability (contact angle) and diffusion studies to show dye distribution were performed. Mechanical and stability assessments were also performed. In addition, release model fitting provided a valuable insight into the potential release mechanism of dyes for the particular and fibrous systems and permeation studies.

2. Materials and Methods

2.1. Materials

PVP (4.4 × 10^4 g/mol, 1.3 x10^6g/mol) was obtained from Ashland, UK, Polycaprolactone (PCL (1.4x10^4,8.0 x10^4g/mol), Ethanol, Dichloromethane, Fluorescein and Rhodamine B (RhB) were supplied by Sigma Aldrich, Dorset, UK, stainless steel microneedles (900 array) was purchased from Adminpatch (California, USA) were all utilised in this study. All reagents were of analytical grade and were purchased from Sigma Aldrich.

2.2. Methods

Implementation of QbD

Identification of quality target product profile and selection of critical quality attributes

The protocol for QbD was applied in this study and examined for dye-loaded MN coatings. In line with implementing QbD to the EHDA process a risk assessment was carried out identifying the factors that can affect the process and the chosen critical quality attributes (CQAs). The foundation of QbD is based on having knowledge to exert control and better understanding of the relationship between CQAs and critical process parameters (CPPs) which are essential for quality target product profile (QTTP). There are many types of risk assessments that can be performed within a QbD framework; examples of such assessments include; cause and effect (fishbone) diagrams, preliminary hazard assessments (PHA) and failure mode and effects analysis (FMEA). According to ICH Q8, QbD implementation begins with identifying the quality target product profile (QTTP) which outlines the quality, safety and efficacy of the product. The QTTP for the four dye-loaded formulations can be found in the appendix. CQAs are defined as a physical, chemical, biological or microbiological property or characteristic that should be within an acceptable limit, range, or distribution to confer the desired product quality. Variability of CPPs has an impact on the CQAs thus the management and control of them are essential. Preliminary studies of solutions enable fixed concentrations being established for the solutions used in the study. EHDA has two main process parameters: the flow rate and the driving force (electric current/voltage). Here, the flow rate was the parameter being investigated. Finally, the design space was identified; determining the optimal conditions.

2.3. *EHDA* and *DOE* analysis

Using JMP software, the DOE was created for each of the polymers (PVP and PCL) to produce structures with desirable shape, size and polydispersity. This was achieved by optimising the EHDA process i.e. altering various process parameters (voltage,

deposition distance and flow rate). A full factorial design was carried out which was able to generate and verify the response surface plots. These plots encompass the interactions between the formulation variables and process parameters to assure quality in the product. Working within the limits of these in theory ensures quality. With a more comprehensive design space/response surface plot, there is ample flexibility within the process parameters.

2.4. JMP Pro Software

Prior to atomisation experiments, JMP software was used to generate the screening design DOE. A full factorial design was then carried out and the responses and factors were input into the system to optimise the system. JMP then analysed all results to statistically explore the data and to visually illustrate the findings. The predictive analytical tools (predictive profilers, response surface plot) which aid to build, enhance and develop a model to predict what will happen with new processes or new risks.

2.5. Solution preparation

Solutions of 1 % w/v and 5% w/v low molecular weight ($4.4x10^4$ g/mol) and high molecular weight PVP ($1.3x10^6$ g/mol) were prepared by dissolving the polymer in ethanol. For the dye loaded formulations a duplicate solution was made with addition of fluorescein dye at 0.05% w/w of PVP concentration.

Solutions of 1 % w/v and 5% w/v low molecular weight PCL ($1.4x10^4$ g/mol) and high molecular weight PCL ($8.0x10^4$ g/mol) were prepared by dissolving the polymer in dichloromethane. For the dye loaded formulations a duplicate solution was made with the addition of Rhodamine B (PCL) dyes at 0.05% w/w of PCL concentration. Table 1 summarises the eight formulations used in this study and their composition.

2.6. Physical characterisation of polymeric solutions

Physical properties (viscosity, surface tension, electrical conductivity and density) of the solutions were examined. Each parameter was tested in triplicate and an average with standard deviation was then calculated. Surface tension was measured using a torsion balance. (White Electrical Instrument, Worcestershire, UK). A Seven Compact S230 conductivity meter (Mettler-Toledo, Switzerland) was used to measure the electrical conductivity of solutions, where prior to each measurement the probe was calibrated using two standards of 1413 S/cm and 12880 S/cm solutions.

Density was obtained using standard 50 mL pyncnometers (VWR, UK). Each pyncnometer was weighed on an analytical balance, filled to full capacity with the solution and then re-weighed. The difference in weight represented the mass (g) of the solution, which was then divided by the volume (25 mL) to get a density value. The following formula is then used to calculate density (Equation 1).

$$Density = \frac{(Weight\ of\ bottle\ and\ formulation - Weight\ of\ Empty\ Bottle)}{Volume\ (25mL)} \quad \text{Eq. 1}$$

Viscosity measurements were recorded at ambient temperature (20.6 ^{o}C) using a SV-10 Sine-wave Vibro viscometer (A&D, Japan). Solutions were poured into a plastic holder and the metal vibrators were clamped down when they had reached the surface of the solution. A reading for viscosity was then recorded and the metal vibrators were cleaned using purified water between each new sample solution reading.

2.7. EHDA – Coating application

A syringe containing 5 mL of formulation was secured to a syringe infusion pump (Harvard apparatus, pump 11-Elite, USA) which controlled the flow rate of polymer-drug solution. The solution then passed through silicon tubing which was connected to a stainless-steel coaxial needle device (single needle was used in this study) at various

199 flow rates (ranging from 15-50 μL/min). This device was attached to a high-power
200 voltage supply (Glassman High Voltage Supply, UK). The ES/ESP process carried out
201 under ambient temperature of 23 °C.
202

203 **2.8. Spraying modes**

204 To assess the various spraying modes, a 5 mL syringe containing solution was ES/ESP
205 at varying voltages (5-15kV) and flow rates (10-80 μL/min) digital images were then
206 taken when different jet formations was observed using a Samsung NX2000 camera.
207

208 **2.9. Preparation of Coated Polymer Microneedles**

209 Microneedles obtained from AdminPatch with an array of 900 needles measured 800
210 μm-tall microneedles located within 1 sq. cm circular area. The entire device is 20 mm
211 in diameter and is made of medical-grade SS316L stainless steel. For the preparation
212 of coated polymer MNs, EHDA was used. The polymeric solution containing the dye
213 was loaded into a syringe fixed to a pump, which allowed the controlled infusion of the
214 solution throughout the system. The syringe was connected to a conducting stainless-
215 steel needle via silicone tubing. The resulting atomised structures were collected on
216 both microscope slides and MNs. Figure 1 shows a schematic diagram of the EHDA
217 set-up.
218

219 **2.10. Imaging analysis**

220 Prior to coating the MNs, solutions containing different concentrations and molecular
221 weights of polymer were atomised at varying flow rates, deposition distances and
222 voltages to assess the morphology and characteristics of the resultant structures. This
223 was according to the QbD DOE experiments. This allowed the most optimal process

parameters to be selected for each formulation. SEM micrographs was taken for these samples including the coated MNs. Prior to analysis, samples were gold coated (S150B, Edwards, Crawley, West Sussex, UK) under vacuum and images were obtained using a Zeiss Evo HD-15 (using an accelerating voltage of 5 kV). Working distances between 9.5 and 10.5 mm were utilised while applied voltages ranged from 10 to 18 kV with magnifications of x5 k and x40 k; termed as low and high magnifications. The optimised samples were observed at low magnification (×40) using Leica DME Optical Microscope using XL1 Camera Software.

2.11. Contact angle analysis

Contact angle of all 8 formulations were characterised using a ThetaLite T100 contact angle goniometer; using OneAttension software to analyse data. 10 µL of distilled water droplets were used. Each sample was carried out and assessed in Sessile Drop mode in triplicate and an average was obtained.

2.12. Particle size analysis

Particle morphology was assessed via a predetermined scale based upon literature records of what is most suitable. Particle size distribution was carried out following SEM analysis. Smart TIFF software was used to measure particle size and fiber diameter. These measurements were then converted into a percentage and the size ranges were plotted as a bar chart to allow for comparison.

2.13. FTIR studies

FTIR was used to analyse all 8 formulations as well as the dyes and raw polymers. Prior to any measurement, FTIR (IRPrestige-21, Japan) background was scanned 10 times

and a range of 400-4000cm^{-1} was determined. The samples were then clamped into place above a dense crystal and scanned ten times. The peaks' wavenumbers were identified and labelled using the Bruker Opus 7.0 FTIR software.

2.14. DSC studies

All 8 formulations as well as the dyes and raw polymers were analysed by Jade DSC (PerkinElmer precisely, Shelton, USA) and Pyris Jade DSC software, to analyse thermal transitions. The sample was placed into an aluminium pan and then covered with a lid with holes, followed by crimping. The sample was loaded into the machine and scanned from 20 °C - 300 °C with a heating and cooling rate of 20 °C/min.

2.15. *In vitro* release studies

Drug release of the optimised nanoparticles were analysed using UV spectroscopy. A phosphate buffered saline (PBS) medium was used to carry it out. Vials containing 10 mL of PBS) and 10 mg of sample (dyes) was constantly stirred at 90 rpm. At predetermined time points, 1 ml of release was retracted and replaced with 1ml of fresh PBS at physiological conditions (37 °C). Drug release was determined using UV spectroscopy absorbance with a set wavelength of $\lambda = 494$ nm (for FL) or $\lambda = 595$ nm (for RhB). This was carried out in triplicate and an average was taken. The data collected from these *in vitro* studies were plotted in different kinetic models to assess the release kinetics of dyes from the atomised polymeric coatings.

2.16. *In vitro* diffusion studies

Transdermal diffusion of dyes was assessed using Franz diffusion cells (Copley Scientific, Nottingham, UK) with a diffusion Surface area of 1.77cm^2. Strat-M®

membrane (purchased from Sigma Aldrich) was first punctured with the coated MN manually for a minimum of 10 seconds (up to 30 seconds) until all needles had penetrated/breached the membrane, it was then removed and the membrane was placed between the donor and receptor compartment (which was filled with 12 mL of PBS and a mini stirrer). The Franz cells were maintained at 37 ± 0.5 °C. An aliquot of 1 mL of sample was withdrawn from the receiver chamber at predetermined intervals and replaced with 1 mL fresh PBS. This receiver solution was agitated using a magnetic stirrer at 400 rpm to ensure homogeneity throughout the experiments. In avoidance of evaporation, the donor cells were covered with parafilm. The experiment was carried out in triplicate for each dye loaded MN. The samples were immediately centrifuged following collection at a speed of 14,000 rpm and the supernatant was analysed. UV spectroscopy (λ = 494/594 nm for PVP/PCL respectively) was used to analyse samples. The cumulative amount of drug permeating through Strat-M® was plotted as a function of time.

2.17. Confocal laser scanning microscope imaging studies

The permeation experiment was carried out for each dye loaded MNs. After 24h, the formulations were removed from the donor compartment and the Strat-M® membranes were removed and wiped gently from the Franz cells. The membranes were placed immediately on a glass slide, covered with a glass slide and examined with laser scanning confocal microscope [46]. Z-stack images were acquired by stepwise scanning of each membrane from its top to the equatorial plane at 1.16 μm steps with a 63× oil-immersion lens under a Zeiss LSM 780 CLSM (Carl Zeiss Microscopy GmbH, Berlin, Germany) with the appropriate filters. Images were obtained with ZEN 2011 software.

2.18. Insertion test of the coated and non-coated MNs

The sufficient insertion ability of the coated MNs is imperative for effective drug delivery into the skin. In the present study, the insertion studies of the uncoated MNs and the coated MNs were performed by using a Testometric tensile test machine (UK) and Parafilm M® (Bemis Company Inc., Soignies, Belgium). Parafilm M® was folded eight times to simulate the thickness of the skin and the MN array was placed onto the movable cylindrical probe with a double-side adhesive tape. The MN arrays were inserted at a speed of 0.5 mm/sec, into the Parafilm layers by applying a force of 40 N for 30 sec. After insertion, the Parafilm layers were unfolded and the number of holes in each layer was counted using an optical microscope (Celestron MicroDirect 1080p HD Handheld Digital Microscope, Celestron, Torrance, California, USA).

3. Results and Discussion

3.1. Evaluation of EHDA process using QbD

The purpose of the first set of experiments was to ascertain which of the two concentrations and molecular weight of polymer should be selected for the production of particles and fibers for each polymer using EHDA (Figure 1). The solutions that were prepared as described in Table 1 were formulated again and each experiment was ES or ESP in the order shown in Figure 2A and B. The factors and responses were put into JMP Pro software and the software generated a table of runs which is displayed in Figure 2. The rationale for these experiments was to produce a full factorial design, whereby parameters that show no desirable responses are eliminated from the remaining DOE providing the next set of experiments.

Once the screening design had been performed and the results analysed, a further verification study was performed. The factors being investigated and their subsequent

ranges were defined further and there were no great variations in the data range. Four sets were carried out, two for the different polymer particles and two for the different polymer fibers. The deposition distance being investigated were 10, 12.5 and 15cm; and 15, 20 and 25 µL/min were the flow rates being looked at for PVP particles and for PCL it was 12.5, 15 and 20 cm; and 20, 40 and 60 µL/min. As can be seen from the initial results, the mean particle size for the majority of the runs were below 500nm as well as the polydispersity results also being low for both particles and for fibers it was within the micron range.

Once the parameters for the particles and fibers were obtained the second set of experiments for PVP and PCL were carried out. The resultant particles/fibers deposited were then assessed using imaging as well as thermal and spectroscopic techniques. The prediction profilers in Figure 2C-F predict the optimal work space regions for the three dependent variables. The response surface plots for particle size are shown in Figure 3A-D and the response surface plots for particle shape and polydispersity can be found in supplementary materials. The implementation and analysis of a response surface fractional factorial DOE with a reduced number of runs helped to identify the effects of the selected independent variables and identify those settings for particles and fibers of optimized quality. The jetting images shown in Figure 4 depicts the various spraying modes. Figure 4A-P show the jetting modes for each formulation.

The appearance of the resulting structures was consistent with all experimental runs producing spherical particles (Figure 5A, B, I, J). High molecular weight PVP shows larger sized structures all within the micrometer range (Figure 5K, L). The polydispersity was also higher with this polymer. The mean particle size was selected as being less than 500 nm; because the aim is to produce nanoparticles any particles produced that are either at this value or lower will meet the criteria that is set in the

QTPP. It has also been stated that nanocarriers that fall into the range of 50-500nm are generally acceptable; it has also been shown that polymeric particles that are <500nm in diameter have a general higher intracellular uptake rate. [47]

At a low flow rate, an array of fibers was produced with varying fiber diameter due to the higher viscosity of the solution. As the flow rate increases, the formation of fibers reduces at the same time as the development of agglomerated material begins to intensify; particularly in Figure 5G. This is due to the short drying time causing non-evaporation of the solvent and low stretching of the solution in the flight between the capillary tip and collector.

Optical images were taken of the finalised formulations which can be seen in Figure 5A-H. The final optimised particles (PVP particles Figure 5I and 5J, PCL particles Figure 5M and 5N) and fibers (PVP fibers Figure 5K and 5L, PCL fibers Figure 5O and 5P). According to the ICH Q8 guidelines a design space can be defined as "the multidimensional combination and interaction of input variables (e.g. Material attributes) and process parameters that have been demonstrated to provide assurance of quality". When working within the designated design space, any change here is not considered by the regulatory authorities as a change in the process therefore this can lead to more flexibility. However; movement out of the design space is considered to be a change and would normally require regulatory approval. Working within the design space guarantees product quality which therefore in turn makes sure that the manufacturing process is robust as well as generating additional financial benefits as there is a reduction in cost as there are less batch failures.

Stability studies of the coated microneedles over time are presented in Figure S1. The resultant particles and fibers were assessed over 10 days. The PVP particles (F2) and the PCL particles (F6) showed no significant morphological changes with no signs of

degradation over a period of 10 days. The same trend was observed with the fibrous structures (F4 and F8). Figure S1 shows the resulting structures at high magnification. Here, the structures have evidently kept their shape and there is no evidence of any morphological changes which is consistent with findings shown in Figure 7. This proves the integrity of polymers and dye and shows that the atomised structures remained intact and stable for an appropriate time period. This also highlights the benefits of the EHDA process; showing that this engineering process is capable of fabricating structures of advantageous morphological and structural stability.

In order to establish a design space the contour profile must have at least two active factors. As can be seen from Figure 3 the prediction profiler flow rate was shown as being an active facor. Therefore in order to obtain a design space for verification studies deposition distance was added to the profile as an active factor.The design space is the white region in the figure and when a process is carried out in this area then producing a product whereby quality is assured.

Flow rate is the only factor that is being shown as having an effect on polydispersity. The p-value is also less than 0.05 indicating that it is important and that an interaction is taking place between polydispersity and the responses being investigated.

Furthermore, the polymers selected demonstrate options for both burst release (PVP) and sustained release (PCL). These polymers have been previously in clinical trials and in current drug dosage form development [48,49]. The study carried out here with these common, compatible polymers also provides imperative evidence that different, potentially personalised structures can be engineered using a method that can be easily optimised for upscaling.

3.2. Physical characterization of solutions

As can be seen in Table 2, the general trend for both high and low molecular weight PVP is that as the concentration of the polymer increases so does the recorded electrical conductivity. The results for electrical conductivity for low and high molecular weight PVP at 5% w/v were all very similar and fell into a very narrow range (3.01 μS/cm and 2.65 μS/cm respectively).

Faraji et al study found that the overall stability of the spraying process is dependent on the electrical conductivity of a sample to a certain extent. It is also believed that an increase in conductivity leads to smaller droplet sizes which occur because during the process there is more of a charge in the liquid solution [50]. Table 2 shows that 1% w/v $1.4x10^3$ g/mol- PCL acquires the highest conductivity value at 7.82 μS/cm and 5% w/v $8x10^3$ g/mol-PCL with the lowest conductivity value at 6.39 μS/cm.

As the viscosity of the solution increases, the surface tension decreases as represented in Table 2 and further confirmed by Abel whom studied the electrospinning of PCL [51]. DCM has shown compatibility with PCL carriers in studies conducted by Xie et al [52]. DCM has a low viscosity of 0.44 μS/cm and low density of 0.166 g/mL and hence has a very insignificant impact on the overall viscosity of the solution.

The formation of fibers is often seen because as the molecular weight of the polymer increased so did the viscosity. This is also to be expected as molecular weight reflects the entanglement of the polymer chains and a higher molecular weight meaning the chains are more rigid and held more tightly together so the viscosity will be much higher when comparing it to lower molecular weight polymers. Similarly, to the electrical conductivity results although error bars were added to the graph they do not show because the standard deviation was far too low at 0.0058 and 0.0153 respectively.

Similarly, to the trend observed in the Table 2 as the concentration of both the high and low molecular weight polymer increased so did the density. The density of polymer

solutions is another important factor that can influence the EHDA process as it dictates whether particles or fibers are going to be produced. It has been thoroughly researched and found that the critical polymer concentration (C_{ov}) can influence the formation of particles. The critical concentration of each polymeric solution can be found; this is when the polymer chain begins to overlap and entangle. In order to produce particles, a low entanglement density is required [53].

Surface tension of a polymeric solution is also another important factor that influences the EHDA process. EHDA is only able to occur when the electric stress is able to overcome the surface tension to form a stable cone jet. This charge repulsion is the rationale for the particle breakdown into nano-sized particles, as the liquid is ejected from the capillary needle and accumulated on the collection plate. The surface tension must be lower than 50 N/m for a liquid to be atomised under the influence of electrical field. The electrical stress must overcome the surface tension to achieve a stable cone-jet. As the surface tension was below this value (50 N/m) for both high and low molecular weight PVP solutions at 0.038 and 0.018 mN/m (high molecular weight PVP at 1% and 5% w/v) and at 0.015 and 0.031 mN/m (low molecular weight PVP at 1% and 5% w/v), it can be assumed that either molecular weight of polymer and concentration (if based solely on surface tension alone) can be used for the EHDA process.

3.3. Spraying modes

Research suggests the most typical spraying modes include dripping, spindle, cone-jet, multi-jet modes depending on the geometrical form of the liquid drop formed at the meniscus/jet at the outlet of the capillary. Other modes of spraying recorded include micro-dripping, multi-spindle, ramified meniscus, oscillating jet and precession have

been observed similarly with a single capillary but dependent upon the liquid and process parameters [54].

The fundamental principle of EHDA involves a liquid emerging from the nozzle under the action of surface tension being subjected to an acceleration force in the form of an electric field. A variety of oscillating behaviours reported in Figure 4 which portrays a range of modes (dripping and jetting). The modes can be very clearly differentiated. The polydispersity index (mean particle size and uniformity of particle size in the distribution can be seen in Figure 4A depends on the spraying mode. The ES droplet can vary from few hundred nanometers to micrometers. Therefore, the physical properties of the solution and experimental design is paramount in the determination of the spraying mode. The EHDA set up was done so with the attachment of a high-speed camera to capture real time live footage of electrospraying and electrospinning in action. Stable cone jets were observed with Figure 4N. The modes were observed from micro-dripping to Taylor cone, as the voltage increases. The map highlights the various regions which includes the different spraying modes and the stable jetting regions. It is in the stable jetting region where a stable cone jet is formed and the resultant spray will lead to the deposition of atomised nanoparticles. The lower viscosity solutions (low polymer weight and lower concentration) yielded smaller droplets and lower polydispersity [55]. The opposing characteristics were found with higher molecular weight and higher concentration polymeric solution, which led to electrospinning with the system [56].

Figure 4J represents the ‘dripping’ mode, which arises when no voltage is applied. Regular, large droplets detach from the capillary to form drops as the electrical force and the weight of the drop overcomes the capillary forces. With a voltage increase, the meniscus elongates and the drop be-comes smaller. The most efficient mode of

attaining a narrow particle size distribution is the 'cone-jet' mode, also known as the stable Taylor cone (Figure 4N). The liquid forms a cone with a thin jet at its apex where the liquid elongates into a long, fine jet and then fragments into droplets under the influence of electrostatic forces. Figure 4P illustrates a 'multi-jet' mode where the meniscus flat-tens with small cones at separate points at the circumference of the capillary, whereby fine jets of liquid are ejected. The 'precession' mode occurs when the liquid escapes the capillary in the form of a skewed cone and changes into a thin jet at its apex (Figure 4I-N). This mode differs from 'cone-jet' as the jet in the 'precession' mode rotates around the capillary axis.

As seen in Figure 4, the formulations containing dye as opposed to polymer alone had distinctive differences. In Figure 4C and Figure 4A there is one consistent unstable region. There was better stability below 15kV. Whereas, in Figure 4D the higher molecular weight polymer with fluorescein dye has a very different jetting map compared to Figure 4B. With F4, the jetting map shown in Figure 4D shows 2 unstable regions making it more problematic to fabricate fibers.

For the PCL formulations, similar behaviour was shown whereby Figure 4E, 4F, 4G and 4H have one unstable region. There is also a larger stable jetting region. Whereas Figure 4F has a large unstable jetting region compared to Figure 4E where there is only a small unstable jetting area for PCL alone. Again, with Figure 4H there are two large unstable jetting regions. It also shows more stable jetting at higher voltages as the flow rate increases.

3.4. Optical microscopy studies

Optical microscopy results show small spherical near uniform particles for both F1 and F2 as shown in Figure 5A and B. Whereas in the optical images for the higher molecular weight formulations Figure 5C has smoother fibers and the PVP-FL fibers shown in

Figure 5D has smooth looking fibers with some beading. This could be due to formulation instability as well as some instability experience during the electrospinning process. This was further confirmed with SEM.

With the optical images obtained for PCL the PCL particles sprayed and shown in Figure 5E the particles are slightly less spherical with some particles agglomerating. Figure 5F shows a larger distribution of particles with some near spherical again with some agglomeration. This can be due to the rapid solvent evaporation as DCM is a very volatile solvent. In Figure 5G there are many beaded fibers with the PCL formulation with more unstable electrospun fibers shown in Figure 5H.

3.5. SEM studies

Figure 5I-P displays the optimised particular and fibrous structures following QbD implementation and DOE analysis. Figure 5I shows uniform, spherical PVP particles and this is similar with the dye loaded PVP-FL particles. Figure 5J was produced at a flow rate of 15 µL/min flow rate and a deposition distance of 15cm were chosen as the optimum conditions to spray. Although the results from JMP show that deposition distance is not an influencing factor literature shows that a greater distance results in smaller particle size; therefore, a deposition distance of 15 cm was selected. Below is an SEM image of the optimised nanoparticles. Similarly, smooth PVP fibers can be seen in both Figure 5K and 5L with the size of fibers measuring very similar. The optimised fibers were produced at a flow rate of 20 µL/min at a deposition distance of 10 cm and the mean fiber size measuring 4.5 µm. The PCL samples were quite problematic to spray initially due to issues with solvent evaporation and agglomeration. However, following DOE analysis, $1.4x10^3$ g/mol-PCL, 5% w/v PCL, a flow rate of 15 µL/min and a deposition distance of 15 cm produced nanoparticles with a mean size of

209nm. The PCL fibers produced in Figure 5O and 5P appear smooth with even distribution compared to that found in the optical images, as these were more stable and produced at optimal conditions at a deposition distance of 10 cm and flow rate of 50 µL/min.

Figure 6 displays the morphology of coated MNs with all 8 formulations. Figure 6A shows sparsely coated MNs with the majority of the coating concentrated at the tips (F1). This is quite similar to what was found with F2. This can also be due to the deposition distance during the spraying process. Figure 6C and 6D display the PVP fiber coated MNs (F3+F4), with the dye loaded MNs appearing as dense as the polymer alone. The fibers appear very dense and smooth on both with Figure 6E and 6F showing a more even coating with PCL particles. The dye loaded F6 PCL particles appear more densely coated (Figure 6F) and Figure 6G shows beaded fibers were present with the polymer alone however more dense coatings with less beading is seen in Figure 6H.

3.6. Size distribution of particular/fibrous structures

The particle size distribution graph for ES PVP and PCL particles shown in Figure 7A are negatively skewed which is desirable. The majority of particles were within the nano size range and this coincides with the polydispersity whereby this value reflects a narrow nanoparticle size distribution with the value closer to 100 nm. This can be seen as important parameters in the QTTP profile (Table S1, S3) and so is a major factor in DOE analysis and the response surface profiles. The average particle size for F1, F2, F5 and F6 were 0.39 µm ± 0.0791 µm, 0.45 µm ± 0.0404 µm, 0.57 µm ± 0.0256 µm and 0.63 µm ± 0.0435 µm, respectively. There was a significantly larger proportion of PCL particles (F5 and F6) within the larger size ranges which could be due to agglomeration as a result of rapid solvent evaporation experienced with DCM.

549 However, on the whole there was a larger frequency of PVP and PCL particles within
550 the smaller size ranges. Research supports these findings as particles with small size
551 distributions have a high level of effectiveness in their application.
552 The average fiber diameter for F3, F4, F7 and F8 1.11 µm ± 0.034 µm, 1.13 µm ± 0.058
553 µm, 1.19 µm ± 0.068 µm and 1.27 ± 0.053 µm. The fiber diameter graph shows even
554 size distribution within the nano and micro range (Figure 7B) which enables them to
555 mimic the extracellular matrix.
556

557 **3.7. Contact angle goniometry studies**

558 Contact angle (CA) has a major impact on drug release from a device/system and the
559 materials surface is the first point of contact with the biological surroundings. It
560 provides quantitative measurements of the wetting of a solid which is liquid (water is
561 commonly used) Angles lower than 90 ° indicate high wettability whilst angles larger
562 than 90 ° indicate poor wettability. CA was necessary in this study to measure the
563 interaction between the polymeric coatings alone and when included with a dye as these
564 varied in structure (particular/fibrous) they would determine the release and detachment
565 from MNs (Figure 8). The wettability of the surface of the electrically atomised samples
566 were characterised and analysed over time. This included hydrophilic (PVP) and
567 hydrophobic (PCL) particles and fibers making it a potential carrier drug delivery
568 system providing controlled rapid/sustained drug release.
569 It has been reported that with increasing molecular weight of PVP that the density
570 increases and the water content decreases. This supports the findings in Figure 8. F3
571 and F4 are the higher molecular weight PVP samples and the contact angle
572 measurements as seen in Figure 8A is much higher at 0 seconds (14.98 ° and 39.01°

respectively) in comparison to the lower molecular weight PVP F1 and F2. PVP is a more hydrophilic polymer hence the rapid dissipation.

PCL has gained its notoriety being easily accessible, easy to process, good mechanical strength and biodegradation. From the results it is apparent that compared to the PCL polymer alone the dye inclusion further increased the contact angle. This is due to the hydrophobicity of PCL which was improved when modified. Its hydrophobicity has a whole host of effects including the adherence of proteins onto a surface thus suggesting optimal contact angle measurements needed for certain applications. Although the surface tension did not vary massively between the PCL formulations, the contact angle for fibers was lower with F8 as their fiber diameter increased more so than F7. F8 is classed as super hydrophobic. The higher CA values in comparison to PVP can also be due to PCL stability and resistance to degradation by the deionized water. It's been reported that the test medium, porosity and test medium can all significantly impact CA behaviour.

3.8. FTIR studies

The FTIR spectrum shown in Figure 9A is that of the pure PVP. Peaks at 3418.88 cm^{-1} (O-H stretch), 2955 cm^{-1} (C-H asymmetric stretch), 1644.36 cm^{-1} (C=O stretch), 1421.22 (CH_2) and 1285.69 cm^{-1} (C-N vibration) are identified which correspond to the structure of PVP.

Figure 9A also displays the spectrum obtained for pure fluorescein and the following peaks identified in the spectrum confirm that the sample being analysed is that of fluorescein. 1636 cm^{-1} (C=O symmetric stretch), 1588.4 cm^{-1} (COO^- asymmetric stretch), 1457.23 cm^{-1} (C-C stretch), 1366.47 cm^{-1} (C-C stretch) and 1108.08 cm^{-1} (C-H

aromatic in plane bend). These peaks and bonds were also identified in an article by Wang *et al.,* when they too were analysing raw fluorescein [54].

The optimised nanoparticles significant peaks include; 3416.14 cm^{-1} (OH stretch), 2953.05 cm^{-1} (CH asymmetric stretch), 1651.33 cm^{-1} (C=O stretch), 1460.96 cm^{-1} (C-C stretch) and 1422.26 cm^{-1} (CH_2 bend). When comparing the spectrum for pure PVP and the optimised nanoparticles they appear to be very similar and the majority of the peaks that were seen in the spectrum for PVP are also visible in the spectrum for the optimised nanoparticles. The peak at 1460.96 cm^{-1} corresponding to the C-C bond is also present in the fluorescein spectrum which can therefore lead to the assumption that fluorescein and PVP have encapsulated together. The peaks also appear much broader and well defined which is often seen in a spectrum when two or more components are believed to be mixed.

In Figure 9B, the characteristic absorption peak at 1730 cm^{-1} is the major transmission peak of PCL and arises due to the carbonyl stretching of the C=O. The bands at 2943, 1293, 1238, 1164, 1107 and 1045 cm^{-1} which correspond to asymmetric CH2 stretching, C-O and C-C stretching in the crystalline phase, asymmetric COC stretching, OC-O stretching, symmetric COC stretching and C-O and C-C stretching in the amorphous phase, respectively. The major peaks are confirmed by Gurlek et al. in 2017 [56]. In Fig. 13b, the weak intensity band at 3085 cm^{-1} denotes to aromatic C-H bonds, which also arises at 1335 cm^{-1} (plane bending), 815 cm^{-1} (out of plane bending) and at 681 cm^{-1} (wagging vibrations). The peaks at 1691 cm^{-1} and 1644 cm^{-1} are associated with the vibrational stretching of C=N and C=O, respectively. The strong band at 1583 cm^{-1} is due to the asymmetric stretching of the COO- group which is further confirmed by the band at 1469 cm^{-1}, ascribed to symmetric stretching of the

group. The aromatic C-C stretch is observed at 1335 cm^{-1} and the C-O results from the 1245 cm^{-1} peak. The major peaks are confirmed by Dukali et al. in 2014 [57].

In addition, the F6 spectra can confirm the interaction between the selected polymer PCL and model compound, RhB. Large similarities between the PCL and F6 and F8 spectra appear. This is due to the RhB becoming encapsulated within the polymeric chains, thus we can observe absorbance resemblances between them. The following transitions in the peaks (peak shifts and broadening) indicate successful interaction between PCL and RhB; the peaks at 2933 cm^{-1} and 1100 cm^{-1} became broader and could be due to the interaction of the peaks of unprocessed RhB at 1583 cm^{-1} and 1073-1175 cm^{-1}, respectively. Additionally, a peak formed at 801 cm^{-1} which is due to the several absorbance at and around 779 $cm^{-1,}$ shown in unprocessed RhB.

3.9. DSC studies

Figure 10A displays the DSC thermogram for pure PVP. As can be seen from the thermogram there is a distinctive peak at 120 °C which represents the melting temperature of the sample. In many sources of literature, it is stated that the melting point of pure PVP should fall in the range of 150 °C-180 °C; however, the melting point recorded does not show this and appears to be out by 30 °C. The sample for pure PVP was analysed again to make sure that the recorded melting point was not an anomalous result; but after repeating this particular run a further two times the melting temperature of 120 °C was still recorded.

This slightly lower melting point value may have been recorded and explained by the fact that the PVP being tested had a molecular weight of 40K; and it has been noted that the molecular weight of a polymer can affect the melting point. This is because an increase or decrease in molecular weight can influence the overall flexibility and/or

646 rigidity of a polymer which can therefore in turn have an effect on the polymers melting
647 point.
648 The melting point for fluorescein is above 300 °C and a clear endothermic peak is
649 visible at 340 °C for FL. It can be seen from the thermogram there is also only one
650 single peak representing the melting point; this observation can be to a certain extent
651 be linked to the purity of the sample as there are no other peaks or interactions being
652 shown. Making sure that the starting materials themselves at the start of a process are
653 pure and therefore of the desired quality is very important when implementing a QbD
654 approach; as in order to make sure that the end product is of exceptional quality each
655 aspect and unit operation of the manufacturing process must also conform to a robust
656 and high-quality procedure.
657 For the optimised nanoparticles the thermogram a single endothermic peak is visible at
658 approximately 120 ºC. This melting point is the same as is seen on the raw PVP
659 thermogram; therefore, it can be assumed that the PVP and fluorescein dye have fully
660 encapsulated and have formed a single entity.
661 DSC provides thermal information about the materials used to facilitate in the
662 identification and verification of excipients. DSC results, presented in Figure 11B,
663 show a single melting peak with a maximum melting temperature (T_m) of unprocessed
664 PCL of ~ 62°C. The T_m of unprocessed RhB is ~ 208 °C and can be seen on the
665 thermogram.
666 However, a second broad peak is observed at ~ 265 °C. The phenomenon of double
667 melting peaks is due to the impartial melting and recrystallisation of the crystallite at
668 that specific moment of thermal scanning. The T_m and second peaks are associated
669 with the melting of imperfect and perfect crystallite, respectively [58]. The T_m of F6
670 and F8 spectra is shown to be slightly decreased (~53 °C), implying that smaller

671 crystallites are formed during EHDA and successful encapsulation of RhB within
672 PCL.
673
674 **3.10. *In vitro* release studies**
675 *In vitro* release study results are shown in Figure 11. The PVP particle (F2) formulation
676 displayed 100% of FL dye was released within 120 minutes (2 hours) with initial burst
677 release similar to the trend shown with (F4) PVP fiber formulations as FL dye showed
678 100% release within 300 seconds (5 h). At 120 minutes, the proportion of drug released
679 was 100%; this satisfies the original QTPP where 75% or more of the drug should have
680 been released before 4 h. At 30 min, approximately 94% of the drug had been released
681 for both F2 and F4; after this point, a plateau had reached as the majority of the drug
682 had already been released. These results are similar to what is reported in literature.
683 Rapid release profiles are associated with PVP with one study reporting up to 100%
684 drug release with PVP coated formulations within 15 min [59]. The slightly longer
685 delay can be attributed to FL. The error bars displayed on the graph above are also
686 narrow suggesting that there was little variation when performing each individual test
687 run and this suggests that the results obtained are both reliable and reproducible.
688 RhB possesses a distinctive and strong absorption peak, which offers an accurate
689 concentration analysis using UV spectroscopy. The initial burst (1 minute) of shows a
690 ~ 44% of RhB being released, which can be observed in Figure 11A**.** An initial burst
691 resulted from the large surface area to volume ratio of the NP, in addition to the surface
692 loading of RhB. From 2 – 10 min, the release gradually increases from ~ 44% to 52%.
693 After 10 min, the drug released slowly with a total of ~ 75% released after 4 h. The
694 delayed release was due to the opposing effects of the hydrophobicity of PCL and
695 hydrophilicity of RhB. This hindered the release of RhB thus presenting a sustained

release profile. Moreover, the QTPP necessitated a sustained release of RhB over a minimum of 7 days. Approximately, 100% of RhB was released after 7 days, which resonates with the QTPP target for the release profile. The release profile was further confirmed by Cao et al in 2014 where the release profile of RhB from PCL/PLGA was measured in a study investigating the 'dual drug release from core-shell nanoparticles [60]. At 7 days, the EE and DL were measured. The calculated values were 65% and 0.6%, respectively. The target EE as stated in the QTPP is > 85%, however only 65% of RhB was successfully encapsulated in PCL. This may because of the unstable jet during ES and ESP, resulting in loss of particles and beaded fibers. The rapid release of PVP formulations in comparison to the sustained release profiles shown with PCL has support from the well documented research of these polymers within the research community.

3.11. Release Kinetics

The data from the in vitro release of dyes was applied to different kinetic models to determine the most prominent mechanism of dyes from the ES/ESP particles/fibers. The data was fitted to zero-order, first-order, Higuchi and Korsmeyer-Peppas models with the regression values and relevant component values being recorded and the corresponding plots seen in Figure 11B-E.

Drug diffusion must occur in one direction with the initial drug concentration in the polymeric matrix must be higher than the solubility of drug. The swelling capability of the polymeric matrix and dissolution must be negligible and the drug particles must be smaller than the matrix. If perfect sink conditions have been met as well as the set criteria then the Higuchi model can be applied.

The Korsmeyer-Peppas model is most useful when there are multiple release mechanisms involved. A release exponent, n, determines the mechanism of drug release. There can be various n values and each depict specific release mechanisms ; $n \leq 0.45$ corresponds to quasi-Fickian drug transport, $n = 0.5$ shows Fickian diffusion (molecular diffusion of drug due to a chemical potential gradient), $0.45 < n < 0.89$ relates a Non-Fickian diffusion mechanism, $n = 0.89$ relates to the case II transport with $n > 0.89$ corresponds to the super case II transport [61].

The low R^2 values (Table 3) obtained from zero-order and first order models suggest a poor fit for this type of release kinetics. There were relatively higher (close to 1) R^2 values for all 4 formulations from Higuchi model analysis which suggests the dyes were released via Fickian diffusion; more specifically quasi-Fickian diffusion. From applying the release data to Korsmeyer-Peppas model the n values for F6 and F8 fall between the 0.5-0.89 ranges and so indicates anomalous case II transport kinetics. The n values for F2 and F4 is >0.89 so it is considered as super case II non- Fickian diffusion [32]. Korsmeyer equation supports the findings for F2 and F4 which have very high (close to 1) n values with research of release from hydrophilic polymers like PVP and the ratio of tracer/excipient. In particular the role of the dynamic swelling and dissolution of the polymeric matrix on the release mechanism [61].

3.12. SEM analysis of Strat-M® membrane and coated microneedles post insertion

Figure 12 displays SEM micrographs of the Strat-M® membranes and the coated MNs that were used for permeation studies. The micrographs show the morphology of the synthetic membrane as well as MNs post insertion. In Figure 12A the membrane appears very smooth and from the side the layers are visible. The pierced membranes in Figure 12Bi), Ci), Di), Ei) show that cavities have been created as the inset pictures

show clear holes created by the microneedles whereby the coating is able to permeate through for permeation and drug delivery. As seen in Figure 12Bi) and Di), there was a limited number of particles surrounding the pierced craters that have been formed; showing the coating had not accumulated here.

In comparison to human skin synthetic membranes offer many advantages including controlled membrane thickness, rapid preparation time, more economic and less storage space. Human SC is usually the rate-limiting step for successful Active Pharmaceutical Ingredient delivery (API). Strat-M® has been designed to encompass similar structural and chemical characteristics found in the human epidermis. This is via the layers in Strat-M® which has a thickness of 300µm. The top layer being supported by 2 layers of porous polyether sulfone (PES) on top of one single layer consisting of polyolefin (non-woven fabric). These multiple layers mimic the layers of human skin. Skin contains various lipids, phospholipids and ceramides, which provides hydrophobicity to skin. Similarly, the membrane contains a combination of lipids (cholesterol, ceramides, free fatty acids and other components) in a specific ratio which is similar to human SC, thus enabling it to be considered as a strong alternative to human skin for permeation studies [62]. Alison et al demonstrated a similar permeation profile of Rivastigmine using Strat-M® compared with pig ear skin [63].

The MNs post insertion shows sparse coating on the majority of MNs. The tips show no coating. There are some particles on Figure 12C and 12G below the tip suggesting not all of the formulation was able to penetrate through the film. MNs hosting fibrous coatings however showed no coating remaining on the MN tips. There is a very small amount of particular-fibrous structures remaining but this supports the phenomena whereby upon insertion, the fibers are dragged through the skin. The integrity of MNs

was significantly different with each MN. MNs coated with F6 (Figure 12G) shows agglomeration of particles potentially due to rapid solvent evaporation.

3.13. Permeation studies

Permeation studies of dyes across a synthetic skin membrane (Strat-M®) *in-vitro* was carried out using coated stainless-steel microneedles. The conclusion of the experiment led to the production of graphs displaying the cumulative amount of model dye permeating the membrane over time (Figure 13). There was a significant difference in the permeation of PVP fibers in comparison to the other formulations and this can be attributed to molecular dispersion of dye within PVP. With the fast swelling of porous nano-sized fibers and large surface area allowing the fluorescein dye to leach out. Research carried out by Ronnader et al supports the findings with a similar release profile with higher molecular weight PVP and sumatriptan loaded MNs [64]. It was also reported that there was a two fold increase in cumulative drug release over a 24 h period by increasing the sumatriptan succinate concentration by a factor of two [65].

In vitro release is not the only issue that can have an impact on skin permeation of a drug. It is also possible that the interaction of the nanoparticles with the SC is responsible for the greater or smaller increase in drug skin permeation. An array of research has been carried out with respect to the behaviour of surfactants and oleic acid as permeation enhancers. Oleic acid has the ability to interact with the ceramide head groups of the SC destroying the hydrogen bonding of the lipid bilayers and in turn enhancing drug skin permeation [66,67].

Hence, structures with two different morphologies were engineered using the same materials. The release study data reflects the effects of particulate and fibrous structures on the controlled release of the encapsulated probe. One limitation or challenge that is

met when utilising MNs as drug delivery device is powder/particle residue on the metal surface post insertion [69]. Fabricating fibrous structures will promote entanglement and forces the coating to be drawn into the pores made by the metal MNs; as seen in Figure 12. The fibrous system could potentially delay the closure of the pores; ensuring the channels are kept open for a longer period of time; increasing drug retention time and hence sustaining drug release. Furthermore, fibrous coatings engineered using electrospinning are easier to manage and handle with being able to control deposition of the resulting structure [69]. It is evident from extensive research surrounding EHDA process synthesises that highly charged droplets and hence charged structures [5]. This can potentially result in repulsion between surfaces of similar charge, ergo fabricating a non-uniform coating, regardless of charge dissipation upon deposition [70-71]. It is important to note here the overall MN coating has the same quantity of particles and fibers required by mass. With respect to particulate deposition, there will be some evident differences when compared to fibrous systems as the latter are more stable [72]. With particle engineering using EHDA, deposition time is significantly increased and with dense coating there is a high probability of static build up; which can be overcome by using grounded electrodes [73].

3.14. Confocal laser scanning microscope imaging

The distribution of Fluorescein and Rhodamine-B in the Strat-M® membrane was visualized confocal laser scanning microscopy (CLSM). The strong green signal is attributed to the fluorescein while the red signal is attributed to Rhodamine-B. CLSM is often used as an imaging technique for further information about transdermal permeation such as the extend and the penetration route. Figure 14 demonstrates Z stack images of the Strat-M® membranes pierced with (A) F2, (B) F4, (C) F6 & (D) F8 MNs.

High fluorescence intensities were maintained across the membrane in all formulations while F8 and F4 seem to have a more intense signal especially in lower depth. CLSM imaging indicates the high potential of the investigated MNs for transdermal delivery. Moreover, Figure 14c reveals the size and shape of the MNs while the tip of the microneedle reaches the lowest depth (z=10).

3.15. Insertion studies

The insertion ability of the coated and non-coated MNs was evaluated using an eight layer Parafilm M® to mimic the skin insertion [74-75]. The average thickness of the Parafilm layer was 127 μm and the percentage of holes created in each layer was calculated using an optical microscope. An average force of 40 N was applied to each MN array for 30 sec and all the MNs perforated the first three layers of the Parafilm. The coated MNs perforated the fifth layer but with a lower percentage of holes (20-25%), while the non-coated MNs reached the sixth layer and the percentage of holes created was up to 22% (Figure S2). All the MNs successfully penetrated the third layer of the Parafilm which corresponds to a penetration depth of 381 μm, indicating that they can reach the skin dermis [76]. The profiles of force versus displacement of F2 and F4 are depicted in Figure S3. The two coated MNs present the same mechanical behavior with a continuous and gradual increase in force, suggesting that they do not deform during insertion. The insertion studies suggest that the MNs subjected to EDHA are capable of transdermal drug delivery.

4. Conclusion

This study demonstrated the effects of different polymeric MN coatings loaded with dye. The resultant ES/ESP particular and fibrous structures were assessed and

characterised. Morphological studies exhibited primarily smooth fibers with some beaded fibers with the PCL formulation and spherical particles. Thermal analysis conferred the stability of nanoparticles and nanofibers with differential scanning calorimetry also showing the dye was molecular distributed in a state throughout the polymeric matrix with all 4 formulations. Spectroscopic studies also confirmed these findings. As the release exponents were between 0.5 and 1, therefore the diffusional release was assumed to follow anomalous transport. The drug skin permeation results showed that the *in-vitro* delivery of dye in the receiver compartment after a few hours was quite high. These results demonstrate that the MN shafts successfully pierced the Strat-M® membrane and dissolved thus releasing a high percentage of their drug load. These results show great promise for the polymers to act as a matrix for model drug. However, permeation can potentially be improved with the inclusion of a permeation enhancer which can enhance drug skin permeation. The application of QbD can add significant value via optimisation of formulations with the most suitable permeation enhancer, polymer and dye/model drug system. Thus, eliminating the need for countless experiments as well as ensuring quality is built into the final product with excellent release profiles and greatly enhanced permeation.

References

[1] M.N. Javed, M.S. Alam, A. Waziri, F.H. Pottoo, A.K. Yadav, M.S. Hasnain, F.A. Almalki, Chapter 12 - QbD Applications for the Development of Nanopharmaceutical Products, in: S. Beg, M.S. Hasnain (Eds.), Pharmaceutical Quality by Design, Academic Press, 2019: pp. 229–253.

869 [2] G. Amasya, B. Aksu, U. Badilli, A. Onay-Besikci, N. Tarimci, QbD guided early
870 pharmaceutical development study: Production of lipid nanoparticles by high pressure
871 homogenization for skin cancer treatment, Int. J. Pharm. 563 (2019) 110–121.
872 [3] E. Ohage, R. Iverson, L. Krummen, R. Taticek, M. Vega, QbD implementation and
873 Post Approval Lifecycle Management (PALM), Biologicals. 44 (2016) 332–340.
874 [4] A. Rezvanpour, W.B. Krantz, C.-H. Wang, Scaling analysis of the
875 electrohydrodynamic atomization (EHDA) process for pharmaceutical particle
876 fabrication, Chem. Eng. Sci. 80 (2012) 81–90.
877 [5] P. Mehta, R. Haj-Ahmad, M. Rasekh, M.S. Arshad, A. Smith, S.M. van der Merwe,
878 X. Li, M.-W. Chang, Z. Ahmad, Pharmaceutical and biomaterial engineering via
879 electrohydrodynamic atomization technologies, Drug. Discov. Today. 22 (2017) 157–
880 165.
881 [6] L. Wang, M. Chang, Z. Ahmad, H. Zheng, J. Li, Mass and controlled fabrication
882 of aligned PVP fibers for matrix type antibiotic drug delivery systems, Chem. Eng. J.
883 307 (2017) 661-669.
884 [7] Z. Ekemen, Z Ahmad, E. Stride, D. Kaplan, M. Edirisinghe,
885 Electrohydrodynamic bubbling: An alternative route to fabricate porous structures of
886 silk fibroin based materials, Biomacromolecules. 14 (2013) 1412-1422.
887 [8] Z. Ekemen, H. Chang, Z. Ahmad, et al. Fabrication of biomaterials via
888 controlled protein bubble generation and manipulation, Biomacromolecules. 12 (2011)
889 4291-4300.
890 [9] S. Kavadiya, P. Biswas, Electrospray deposition of biomolecules: Applications,
891 challenges, and recommendations, J. Aerosol. Sci. 125 (2018) 182–207.

892 [10] T.H. Hwang, Y.J. Kim, H. Chung, W. Ryu, Motionless Electrohydrodynamic
893 (EHD) Printing of Biodegradable Polymer Micro Patterns, Microelectron Eng. 161
894 (2016) 43–51.
895 [11] J.L. Li, On the meniscus deformation when the pulsed voltage is applied, J.
896 Electrostat. 64 (2006) 44–52.
897 [12] P. Mehta, H. Picken, C. White, K. Howarth, K. Langridge, K. Nazari, P. Taylor,
898 O. Qutachi, M.W. Chang, Z. Ahmad, Engineering optimisation of commercial
899 facemask formulations capable of improving skin moisturisation, Int. J. Cosmet. Sci.
900 41 (2019) 462–471.
901 [13] J Wang, M. Chang, Z. Ahmad, J. Li, Fabrication of patterned polymer-antibiotic
902 composite fibers via electrohydrodynamic (EHD) printing, J. Drug. Deliv. Sci. Technol.
903 35 (2016)114-123.
904 [14] R. Bakhshi, Z. Ahmad, M. Soric, E. Stride, M. Edirisinghe, Nanoparticle
905 delivery systems formed using electrically sprayed co-flowing excipients and active
906 agent, J. Biomed. Nanotechnol. 7 (2011) 782-793.
907 [15] Y. Echegoyen, M.J. Fabra, J.L. Castro-Mayorga, A. Cherpinski, J.M. Lagaron,
908 High throughput electro-hydrodynamic processing in food encapsulation and food
909 packaging applications: Viewpoint, Trends. Food. Sci. Technol. 60 (2017) 71–79.
910 [16] Z. Yao, L. Jin, Z Ahmad, J. Huang, M. Chang, J. Li, Ganoderma lucidum
911 polysaccharide loaded sodium alginate micro-particles prepared via electrospraying in
912 controlled deposition environments, Int. J. Pharm. 524 (2017) 148-158.
913 [17] M. Nangrejo, Z. Ahmad, E. Stride, M. Edirisinghe, P. Colombo. Preparation of
914 polymeric and ceramic porous capsules by a novel electrohydrodynamic process,
915 Pharm. Dev. Technol. 13 (2008) 425-432.

916 [18] E. Sayed, C. Karavasili, K. Ruparelia, et al. Electrosprayed mesoporous
917 particles for improved aqueous solubility of a poorly water soluble anticancer agent: In
918 vitro and ex vivo evaluation, J. Control. Release. 278 (2018) 142-155.
919 [19] P. Toman, C. Lien, Z. Ahmad, et al. Nanoparticles of alkylglyceryl-dextran-
920 graft-poly(lactic acid) for drug delivery to the brain: Preparation and in vitro
921 investigation, Acta. Biomater. 23 (2015) 250-262.
922 [20] K. Nazari, E. Kontogiannidou, R.H. Ahmad, et al. Development and
923 characterisation of cellulose based electrospun mats for buccal delivery of non-steroidal
924 anti-inflammatory drug (NSAID), Eur. J. Pharm. Sci. 102 (2017) 147-155.
925 [21] O. Gunduz, C. Gode, Z. Ahmad, et al. Preparation and evaluation of cerium
926 oxide-bovine hydroxyapatite composites for biomedical engineering applications. *J*
927 *Mech Behav Biomed Mater*. 2014;35:70-76.
928 [22] X. Li, J. Huang, Z. Ahmad, M. Edirisinghe. Electrohydrodynamic coating of
929 metal with nano-sized hydroxyapatite, Biomed Mater Eng. 17 (2007) 335-346.
930 [23] M. Hwan-Lee, S. Lee, Bioprospecting potential of the soil metagenome: Novel
931 enzymes and bioactivities, Genomics.Inform. 11 (2013) 114-120.
932 [24] Z. Ahmad, J. Huang, M. Edirisinghe, et al. Electrohydrodynamic print-
933 patterning of nano-hydroxyapatite, J. Biomed. Nanotechnol. 2 (2006) 201-207.
934 [25] Y. Gao, Y. Bai, D. Zhao, M. Chang, Z Ahmad, J. Li, Tuning microparticle
935 porosity during single needle electrospraying synthesis via a non-solvent-based
936 physicochemical approach, Polymers. 7 (2015) 2701-2710.
937 [26] P, Mehta, A.A Al-Kinani, R. Haj-Ahmad, M.S. Arshad, M.W. Chang, R.G. Alany,
938 Z. Ahmad, Electrically atomised formulations of timolol maleate for direct and on-
939 demand ocular lens coatings. Eur. J. Pharm. Biopharm. 119 (2017) 170-184

[27] J.C. Wang, H. Zheng, M.W. Chang, Z. Ahmad, J.S. Li, Preparation of active 3D film patches via aligned fiber electrohydrodynamic (EHD) printing. Sci Rep. 8 (2017) 43924.

[28] G. Aditya, D. Parmeshwar, S. Mukty, Nanofiberous coating for Bare Metal Stents: A comparative study of coaxial and monoaxial modes, Mater. Today. Proc. 18 (2019), 1108 -1115

[29] A. Smeets, C. Clasen, G. Van den Mooter, Electrospraying of polymer solutions: Study of formulation and process parameters, Eur J Pharm Biopharm. 119 (2017) 114–124.

[30] R. Ali, P. Mehta, I. Kucuk, M. Chang, Z Ahmad. Transdermal Microneedles-A materials perspective. AAPS PharmSciTech. 21 (2019) 12

[31] M. Nurunnabi, V. Revuri, K.M. Huh, Y. Lee, Chapter 14 - Polysaccharide based nano/microformulation: an effective and versatile oral drug delivery system, in: E. Andronescu, A.M. Grumezescu (Eds.), Nanostructures for Oral Medicine, Elsevier, 2017: pp. 409–433.

[32] C. Dillon, H. Hughes, N.J. O'Reilly, C.J. Allender, D.A. Barrow, P. McLoughlin, Dissolving microneedle based transdermal delivery of therapeutic peptide analogues, Int. J. Pharm. 565 (2019) 9–19.

[33] S. Sharma, K. Hatware, P. Bhadane, S. Sindhikar, D.K. Mishra, Recent advances in microneedle composites for biomedical applications: Advanced drug delivery technologies, Mat. Sci. Eng. C. 103 (2019) 109717.

[34] A.H. Sabri, J. Ogilvie, K. Abdulhamid, V. Shpadaruk, J. McKenna, J. Segal, D.J. Scurr, M. Marlow, Expanding the applications of microneedles in dermatology, Eur. J. Pharm. Biopharm. 140 (2019) 121–140.

964 [35] H.S. Gill, D.D. Denson, B.A. Burris, M.R. Prausnitz, Effect of microneedle
965 design on pain in human volunteers, Clin. J. Pain. 24 (2008) 585–594.
966 [36] P. Ronnander, L. Simon, H. Spilgies, A. Koch, Modelling the in-vitro dissolution
967 and release of sumatriptan succinate from polyvinylpyrrolidone-based microneedles,
968 Eur. J. Pharm Sci. 125 (2018) 54–63.
969 [37] C.L. Caudill, J.L. Perry, S. Tian, J.C. Luft, J.M. DESIMONE, Spatially controlled
970 coating of continuous liquid interface production microneedles for transdermal protein
971 delivery, J. Control. Release. 284 (2018) 122–132.
972 [38] X. Zhao, S.A. Coulman, S.J. Hanna, F.S. Wong, C.M. Dayan, J.C. Birchall,
973 Formulation of hydrophobic peptides for skin delivery via coated microneedles, J.
974 Control. Release. 265 (2017) 2–13.
975 [39] S. Bhatnagar, N.G. Bankar, M.V. Kulkarni, V.V.K. Venuganti, Dissolvable
976 microneedle patch containing doxorubicin and docetaxel is effective in 4T1
977 xenografted breast cancer mouse model, Int. J. Pharm. 556 (2019) 263–275.
978 [40] S.N. Economidou, C.P.P. Pere, A. Reid, Md.J. Uddin, J.F.C. Windmill, D.A.
979 Lamprou, D. Douroumis, 3D printed microneedle patches using stereolithography
980 (SLA) for intradermal insulin delivery, Mat Sci Eng C. 102 (2019) 743–755.
981 [41] H. Khan, P. Mehta, H. Msallam, D. Armitage, Z. Ahmad, Smart microneedle
982 coatings for controlled delivery and biomedical analysis. J. Drug. Target. 22 (2014)
983 790-795.
984 [42] D. Liu, B. Yu, G. Jiang, W. Yu, Y. Zhang, B. Xu, Fabrication of composite
985 microneedles integrated with insulin-loaded CaCO3 microparticles and PVP for
986 transdermal delivery in diabetic rats, Mat. Sci. Eng. C. 90 (2018) 180–188.
987 [43] R. Pranav Kumar Shadamarshan, H. Balaji, H.S. Rao, K. Balagangadharan, S.
988 Viji Chandran, N. Selvamurugan, Fabrication of PCL/PVP Electrospun Fibers loaded

989 with Trans-anethole for Bone Regeneration in vitro, Colloid. Surface. B. 171 (2018)
990 698–706.
991 [44] R.P. Reksamunandar, D. Edikresnha, M.M. Munir, S. Damayanti, Khairurrijal,
992 Encapsulation of β-carotene in poly(vinylpyrrolidone) (PVP) by Electrospinning
993 Technique, Procedia. Eng. 170 (2017) 19–23.
994 [45] T.E. Andersen, A.J. Andersen, R.S. Petersen, L.H. Nielsen, S.S. Keller, Drug
995 loaded biodegradable polymer microneedles fabricated by hot embossing,
996 Microelectron. Eng. 195 (2018) 57–61.
997 [46] S.M. Abdel-Hafez, R.M. Hathout, O.A. Sammour, Tracking the transdermal
998 penetration pathways of optimized curcumin-loaded chitosan nanoparticles via
999 confocal laser scanning microscopy, Int. J. Biol Macromol. 108 (2018) 753–764.
1000 [47] D. Lombardo, M.A. Kiselev, M.T. Caccamo, Smart Nanoparticles for Drug
1001 Delivery Application: Development of Versatile Nanocarrier Platforms in
1002 Biotechnology and Nanomedicine, J. Nanomater. 2019 (2019). 26
1003 [48] M. Teodorescu, M. Bercea, Poly(vinylpyrrolidone) - A Versatile Polymer for
1004 Biomedical and Beyond Medical Applications, Polym. Plast. Technol. Eng. 9 (2015)
1005 923-943
1006 [49] A, Fuchs, A. Youssef, A, Seher, G. Hochleitner, P.D. Dalton, S. Hartmann, R.C.
1007 Brands, U.D.A. Müller-Richter, C. Linz, Medical-grade polycaprolactone scaffolds
1008 made by melt electrospinning writing for oral bone regeneration - a pilot study in vitro.
1009 BMC. Oral. Health. 19 (2019) 28
1010 [50] S. Faraji, B. Sadri, B. Vajdi Hokmabad, N. Jadidoleslam, E. Esmaeilzadeh,
1011 Experimental study on the role of electrical conductivity in pulsating modes of
1012 electrospraying, Exp. Therm. Fluid. Sci. 81 (2017) 327–335.

[51] S. Bongiovanni Abel, L. Liverani, A.R. Boccaccini, G.A. Abraham, Effect of benign solvents composition on poly(ε-caprolactone) electrospun fiber properties, Mater. Lett. 245 (2019) 86–89.

[52] J. Xie, J. Jiang, P. Davoodi, M.P. Srinivasan, C.-H. Wang, Electrohydrodynamic atomization: A two-decade effort to produce and process micro-/nanoparticulate materials, Chem. Eng. Sci. 125 (2015) 32–57.

[53] J. Wang, J.A. Jansen, F. Yang, Electrospraying: Possibilities and Challenges of Engineering Carriers for Biomedical Applications—A Mini Review, Front . Chem. 7 (2019) 258.

[54] Z. Wang, L. Xia, S. Zhan, Experimental study on electrohydrodynamics (EHD) spraying of ethanol with double-capillary, Appl. Therm. Eng. 120 (2017) 474–483.

[55] N.T. Le, J.M. Myrick, T. Seigle, P.T. Huynh, S. Krishnan, Mapping electrospray modes and droplet size distributions for chitosan solutions in unentangled and entangled concentration regimes, Adv. Powder. Technol. 29 (2018) 3007–3021.

[56] A.C. Gurlek, B. Sevinc, E. Bayrak, C. Erisken, Synthesis and characterization of polycaprolactone for anterior cruciate ligament regeneration, Mat. Sci. Eng. C. 71 (2017) 820–826.

[57] R. Dukali, I. Radovic, D. Stojanovic, D. Sevic, V. Radojevic, D. Jocic, R. Aleksic, Electrospinning of laser dye Rhodamine B-doped poly(methyl methacrylate) nanofibers, J. Serb. Chem. Soc. 79 (2014) 867–880.

[58] H. Chen, C. Su, G. Shi, G. Liu, D. Wang, Nature of the double melting peaks of regioregular poly(3-dodecylthiophene), Eur. Polym. J. 99 (2018) 284–288.

[59] S.G. Gumaste, B.O.S. Freire, A.T.M. Serajuddin, Development of solid SEDDS, VI: Effect of precoating of Neusilin® US2 with PVP on drug release from

adsorbed self-emulsifying lipid-based formulations, Eur. J. Pharm Sci. 110 (2017) 124–133.

[60] Y. Cao, B. Wang, Y. Wang, D. Lou, Dual Drug Release from Core–Shell Nanoparticles with Distinct Release Profiles, J. Pharm. Sci. 103 (2014) 3205–3216.

[61] R.W. Korsmeyer, R. Gurny, E. Doelker, P. Buri, N.A. Peppas, Mechanisms of solute release from porous hydrophilic polymers, Int. J. Pharm. 15 (1983) 25–35.

[62] A. Haq, B. Goodyear, D. Ameen, V. Joshi, B. Michniak-Kohn, Strat-M® synthetic membrane: Permeability comparison to human cadaver skin, Int. J. Pharm. 547 (2018) 432–437.

[63] A. Simon, M.I. Amaro, A.M. Healy, L.M. Cabral, V.P. de Sousa, Comparative evaluation of rivastigmine permeation from a transdermal system in the Franz cell using synthetic membranes and pig ear skin with in vivo-in vitro correlation, Int. J. Pharm. 512 (2016) 234–241.

[64] R.N. Kamble, S. Gaikwad, A. Maske, S.S. Patil, Fabrication of electrospun nanofibres of BCS II drug for enhanced dissolution and permeation across skin, J. Adv Res. 7 (2016) 483–489.

[65] P. Ronnander, L. Simon, H. Spilgies, A. Koch, S. Scherr, Dissolving polyvinylpyrrolidone-based microneedle systems for in-vitro delivery of sumatriptan succinate, Eur. J. Pharm. Sci. 114 (2018) 84–92.

[66] P.B.R. da Rocha, B. dos S. Souza, L.M. Andrade, J.L.V. dos Anjos, S.A. Mendanha, A. Alonso, R.N. Marreto, S.F. Taveira, Enhanced asiaticoside skin permeation by Centella asiatica-loaded lipid nanoparticles: Effects of extract type and study of stratum corneum lipid dynamics, J. Drug. Deliv. Sci Technol. 50 (2019) 305–312.

[67] R.M. Hathout, A.H. Elshafeey, Development and characterization of colloidal soft nano-carriers for transdermal delivery and bioavailability enhancement of an angiotensin II receptor blocker, Eur. J. Pharm. Biopharm. 82 (2012) 230–240.

[68] R.S. J. Ingrole, H.S.Gill Microneedle Coating Methods: A Review with a Perspective, J. Pharmacol, Exp. Ther. 370 (2019) 555-569

[69] P. Mehta, A. Zaman, A. Smith, M. Rasekh, R. Haj-Ahmad, M. S. Arshad, S.van der Merwe, M.W. Chang, and Z. Ahmad, Broad Scale and Structure Fabrication of Healthcare Materials for Drug and Emerging Therapies via Electrohydrodynamic Techniques, Adv Ther. 2 (2019) 1800024

[70] V.T. Dau, T.K. Nguyen, D.V. Dao, Charge reduced nanoparticles by sub-kHz ac electrohydrodynamic atomization toward drug delivery applications, Appl. Phys. Lett. 116 (2020) 023703

[71] Z.C. Yao, J.C. Wang, B. Wang, Z. Ahmad, J.S. Li, M.W. Chang, A novel approach for tailored medicines: Direct writing of Janus fibers, J. Drug Deliv. Sci. Technol. 50 (2019) 372-379

[72] H.L. Schreuder-Gibson, P. Gibson Cooperative Charging Effects of Fibers from Electrospinning of Electrically Dissimilar Polymers Int. Nonwovens. J. 13 (2004) 39-45.

[73] M. Rasekh, A. Smith, M.S, Arshad, O. Gunduz, S.M. Van der Merwe, G. Smith, Z. Ahmad, Electrohydrodynamic Preparation of Nanomedicines, Curr. Top. Med. Chem. 15 (2015) 2316-2327

[74] E. Larrañeta, J. Moore, E.M. Vicente-Pérez, P. González-Vázquez, R. Lutton, A.D. Woolfson, R.F. Donnelly, A proposed model membrane and test method for microneedle insertion studies, Int. J. Pharm. 472 (2014) 65–73.

[75] Z. Chen, B. Han, L. Liao, X. Hu, Q. Hu, Y. Gao, Y. Qiu, Enhanced transdermal delivery of polydatin via a combination of inclusion complexes and dissolving microneedles for treatment of acute gout arthritis, J. Drug. Deliv. Sci. Technol. 55 (2020) 101487.

[76] D.F.S. Fonseca, P.C. Costa, I.F. Almeida, P. Dias-Pereira, I. Correia-Sá, V. Bastos, H. Oliveira, M. Duarte-Araújo, M. Morato, C. Vilela, A.J.D. Silvestre, C.S.R. Freire, Pullulan microneedle patches for the efficient transdermal administration of insulin envisioning diabetes treatment, Carbohydr. Polym. 241 (2020) 116314.

Electrospinning/Electrospraying coatings for metal microneedles: a design of experiments (DOE) and Quality by Design (QbD) approach

Radeyah Ali[1], Prina Mehta[1], Paraskevi Kyriaki Monou[2] Muhammad S. Arshad[1], Emmanuel Panteris[3], Manoochehr Rasekh[1], Neenu Singh[1], Omar Qutachi[1], Philippe Wilson[4], Dimitrios Tzetzis[5], Ming-Wei Chang[6], Dimitris G. Fatouros[2], Zeeshan Ahmad[1,*]

[1]Leicester School of Pharmacy, De Montfort University, Leicester, LE1 9BH, UK

[2]Department of Pharmaceutical Technology, School of Pharmacy, Aristotle University of Thessalooniki, Greece.

[3]Department of Botany, School of Biology, Aristotle University of Thessaloniki, GR-54124 Thessaloniki, Greece

[4]School of Animal, Rural and Environmental Sciences, Nottingham Trent University, Brackenhurst Campus, Southwell, NG25 0QF

[5]School of Science and Technology, International Hellenic University, Thermi, Greece

[6]Nanotechnology and Integrated Bioengineering Centre, University of Ulster, Jordanstown Campus, Newtownabbey, BT37 0QB, Northern Ireland, UK

Corresponding authors:

Prof. Dimitrios G. Fatouros e-mail: dfatouro@pharm.auth.gr

Prof. Zeeshan Ahmad e-mail: zahmad@dmu.ac.uk

1139 **Table S1.** QTPP for fluorescein nanoparticles.

Quality Attribute	Target	Critical (Y/N)
Dosage form	Nano particles to be sprayed onto stainless steel microneedles	N
Mode of admistration	Coated Microneedle	N
Route of adminstration	Transdermal	N
Appearance	Spherical particles	Y
Assay	95% - 105%	Y
Identity	Positive for API (fluoroscein)	Y
Release profile	>75% released in 4 hours	Y
Encapsulation efficiency	>80%	Y
Particle size	< 500nm	Y
Polydispersity	< 0.3	Y

1140

1141

1142 **Table S2.** QTPP for fluorescein nano-micro fibers.

Quality Attribute	Target	Critical (Y/N)
Dosage form	Nano-micro fibers to be spun onto stainless steel microneedles	N
Mode of admistration	Coated Microneedle	N
Route of adminstration	Transdermal	N
Appearance	Smooth fibers	Y
Assay	95% - 105%	Y
Identity	Positive for API (fluoroscein)	Y
Release profile	TBD	Y
Encapsulation efficiency	>80%	Y
Particle size	< 2um	Y
Polydispersity		Y

1143

Table S3. QTTP for Rhodamine B nanoparticles.

Product Attribute	Target	Criticality
Route of Administration	Transdermal	No
Dosage Form	Dye loaded nanoparticles sprayed onto stainless steel MN	No
Active	Rhodamine-B dye (model drug)	No
Polymeric Carrier	PCL (Polycaprolactone)	No
Solvent	DCM (Dichloromethane)	No
Release Profile	Sustained release over a minimum of 7 days	Yes
Particle Size	1 - 500 nm	Yes
Particle Shape*	0 – 10	Yes
Poly-Dispersity Index	> 85 %	Yes
Encapsulation efficiency	> 80 %	Yes
Coating Method	EHDA process	No

Table S4. QTTP for Rhodamine B nano-micro fibers

Product Attribute	Target	Criticality
Route of Administration	Transdermal	No
Dosage Form	Dye loaded nano-micro fibers spun onto stainless steel MN	No
Active	Rhodamine-B dye (model drug)	No
Polymeric Carrier	PCL (Polycaprolactone)	No
Solvent	DCM (Dichloromethane)	No
Release Profile	Sustained release over a minimum of 7 days	Yes
Particle Size	0.5-2 um	Yes
Particle Shape*	0 – 10	Yes
Poly-Dispersity Index	> 85 %	Yes
Encapsulation efficiency	> 80 %	Yes

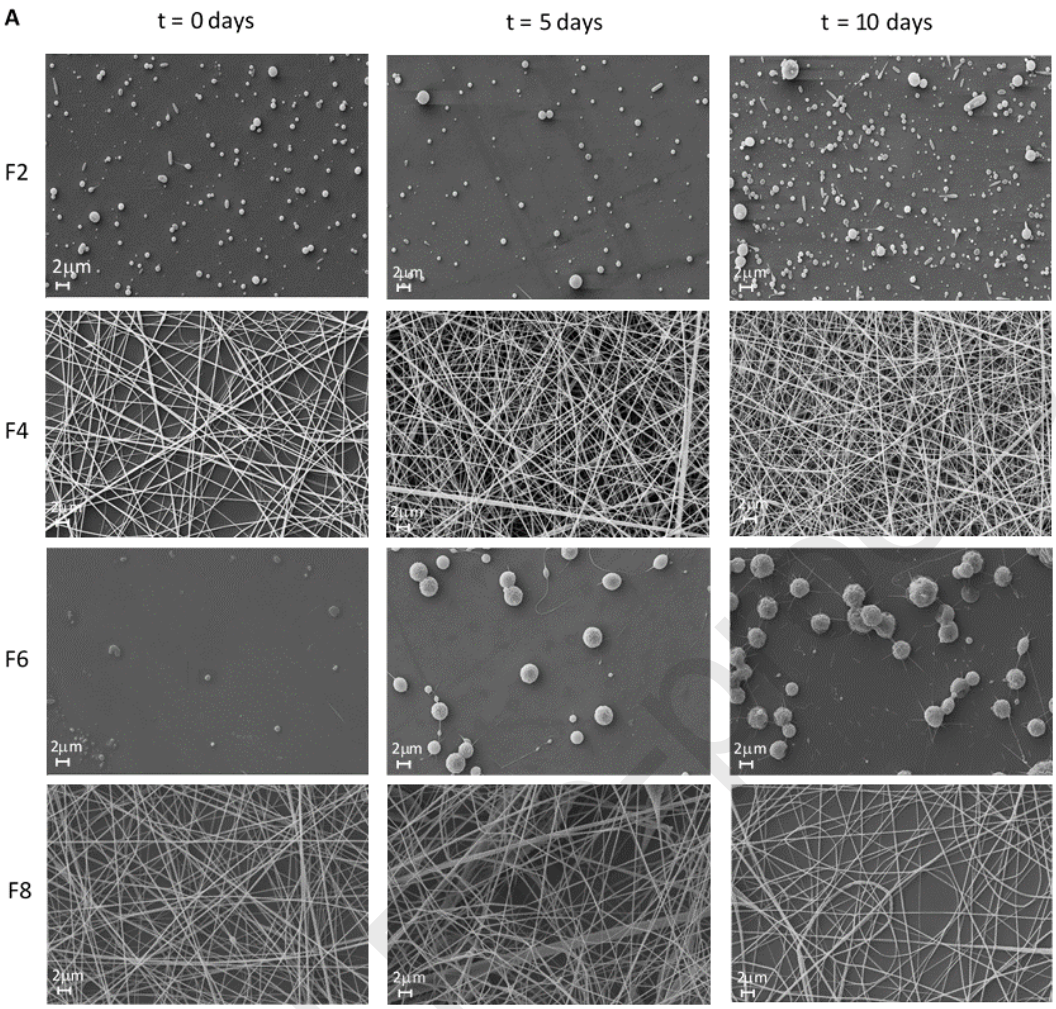

1178

1179

1180

1181

1182

1183

1184

1185

1186

1187

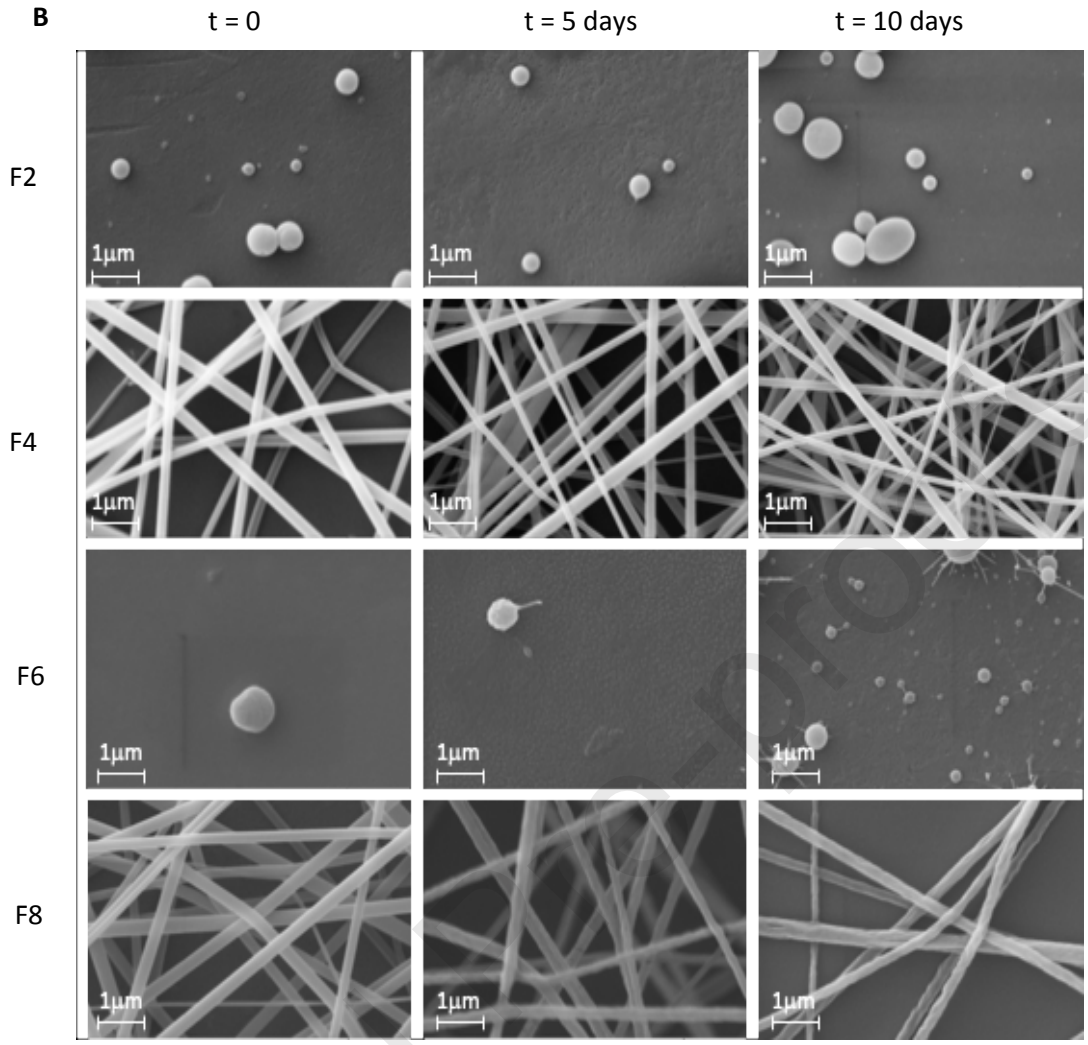

Figure S1: SEM images showing the stability of polymeric particles and fibers over 10 days at A) x5k magnification and B) x40k magnification.

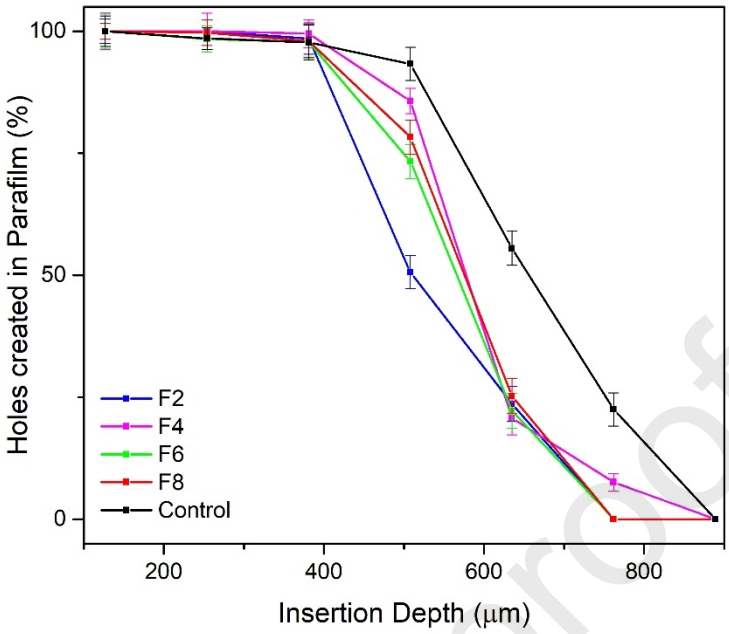

(b)

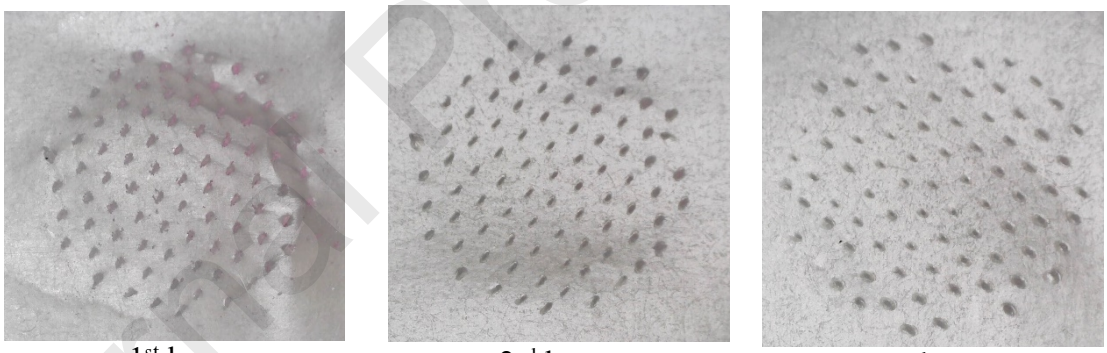

Figure S2. (a) Insertion of F2, F4, F6, F8 and non-coated MNs (control sample) into a model membrane for skin insertion using Parafilm M®. (b) Photos of the first, second and third Parafilm M® layer after insertion of F8 MNs.

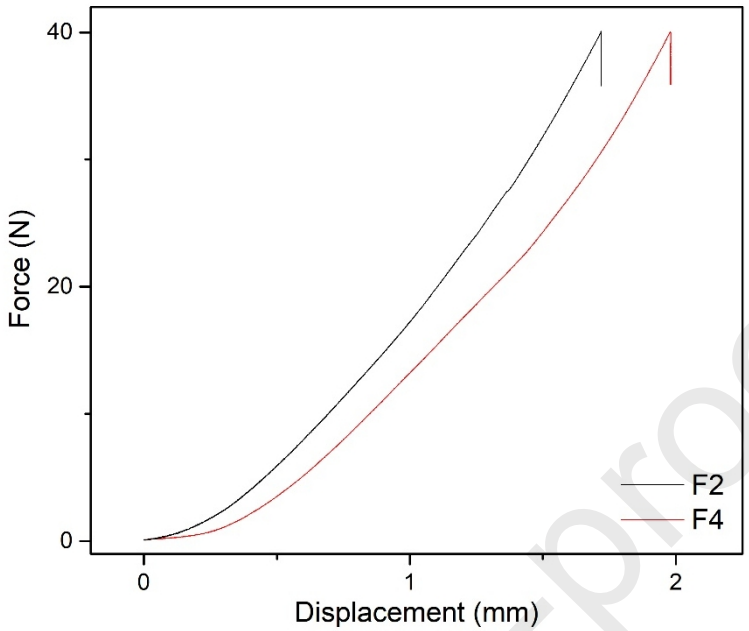

Figure S3. Force-displacement curves of coated MNs F2 and F4 under an axial force load.